Near-field radiative heat transfer in graphene plasmonic nanodisk dimers

Francisco V. Ramirez, Sheng Shen, and Alan J. H. McGaughey*
Department of Mechanical Engineering, Carnegie Mellon University, Pittsburgh, Pennsylvania 15213, USA
(Received 13 May 2017; published 16 October 2017)

Near-field thermal radiation mediated by surface plasmons in parallel graphene nanodisk dimers is studied using a semianalytical model under the electrostatic approximation. The radiative heat transfer between two disks as a function of the distance between them in coaxial and coplanar configurations is first considered. Three regimes are identified and their extents determined using nondimensional analysis. When the edge-to-edge separation is smaller than the disk diameter, near-field coupling and surface plasmon hybridization lead to an enhancement of the radiative heat transfer by up to four orders of magnitude compared to the Planck blackbody limit. A mismatch in the disk diameters affects the plasmonic mode hybridization and can either diminish or enhance the near-field radiation. Destructive interference between eigenmodes that emerge when the relative orientation between disks is varied can induce a twofold reduction in the radiative heat transfer. In all configurations, the radiative heat transfer properties can be controlled by tuning the disk size/orientation, the substrate optical properties, and graphene's doping concentration and electron mobility.

DOI: 10.1103/PhysRevB.96.165427

I. INTRODUCTION

Radiative heat transfer between two bodies separated by a subwavelength gap is called near-field radiation. In this regime, tunneling of evanescent electromagnetic waves leads to heat transfer rates beyond the Planck blackbody limit [1]. The enhancement can be several orders of magnitude in materials that support surface electromagnetic modes, providing that their activation energies are comparable to $k_B T$, where k_B is the Boltzmann constant and T is temperature. Thus, polar dielectrics such as SiO_2 and SiC, which support surface phonon-polaritons in the near-infrared part of the spectrum, demonstrate near-field radiation enhancement at room temperature [2,3]. The near-field thermal radiation response of a bulk material can be modified when it is nanostructured into subwavelength geometries [4–7]. This technique has been explored in metamaterials for tunable near-field thermal radiation enhancement [8–11] and in photon-based solid-state thermal devices [12–15].

Graphene plasmonics has emerged as an alternative platform for strong near-field radiation enhancement [16–19], with potential application in heat flux splitting [13], thermal plasmonic interconnects [20], and ultrafast radiative cooling [21]. The linear electronic dispersion of graphene leads to a high electron mobility and allows for the induction of free carriers by chemical doping or electrical gating [22]. The resulting plasmons are long-propagating and strongly confined, with tunable frequencies from the terahertz toward the midinfrared part of the spectrum [23]. The near-field thermal radiation properties of nanostructured graphene are largely unexplored. Numerical simulations are computationally expensive [24], and studies have been limited to theoretical approaches, such as the point dipole approximation [13] and perturbation theory [25], which are restricted to large separation gaps.

Herein, we study the near-field thermal radiation properties of surface plasmons in dimers built from parallel graphene nanodisks. We use a semianalytical model under the electrostatic approximation, which is suitable when the disk size is smaller than the wavelength of the electromagnetic waves in the surrounding media [26–28]. Our model extends the theory for a single disk developed by Fetter [29] to include analytical expressions for the Coulombic disk-to-disk interactions. Radiative heat transfer is modeled under a fluctuating surface charge formalism that results in a compact expression that uses the coupling matrices developed in the electrostatic formulation. We are thus able to capture near-field coupling at very small gaps with high accuracy. As the electrostatic theory in based on analytical expressions, we are able to obtain results two orders of magnitude faster than numerical simulations based on the boundary element method (BEM) [30]. Because our solution is based in the hydrodynamic theory of two dimensional electron gas [29], the formalism developed here can be extended to other graphene nanostructures such as antidots systems [31], nanorings [32], and nanoribbons [33].

The remainder of the paper is organized as follows. The mathematical formulation is described in Sec. II. The hybridization of surface plasmon modes on disk dimers in coaxial and coplanar configurations is presented in Sec. III A. Near-field radiative heat transfer in these two configurations is then examined in Secs. III B and III C, and the effect of mismatched diameters is considered in Sec. III D. In Sec. III E, the effect of the orientation between the two disks is studied. The results are summarized in Sec. IV.

II. METHODS

Graphene's plasmonic properties are directly related to its optical conductivity, which in the local limit (i.e., negligible spatial dispersion) reduces to [34]

$$\sigma(\omega) = \frac{2e^2 k_B T}{\pi\hbar^2}\frac{i}{\omega + i\tau^{-1}}\ln[2\cosh(E_f/2k_B T)] + \frac{e^2}{4\hbar}\left[H(\omega/2) + \frac{4i\omega}{\pi}\int_0^\infty \frac{H(x) - H(\omega/2)}{\omega^2 - 4x^2}dx\right], \quad (1)$$

*mcgaughey@cmu.edu

 ©2017 American Physical Society

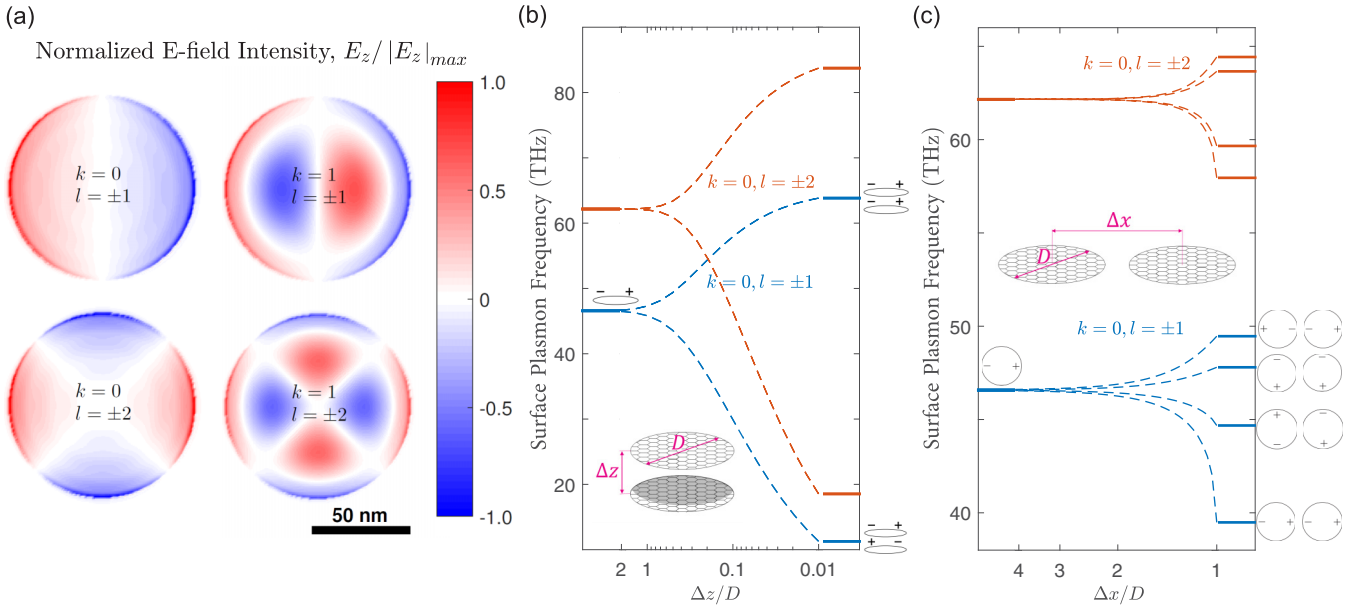

FIG. 1. (a) Real part of the normalized electric-field intensity in the direction perpendicular to the plane of the disk, $E_z/|E_z|_{\max}$, showing the surface charge distribution of the localized surface plasmon modes $(k,l) = (0,\pm1)$, $(0,\pm2)$, $(1,\pm1)$, and $(1,\pm2)$ in an isolated graphene disk ($D = 100$ nm, $E_f = 0.6$ eV). Hybrid surface plasmon resonant frequencies of two graphene nanodisks in (b) coaxial and (c) coplanar configurations as a function of the gap between them ($D = 100$ nm, $E_f = 0.6$ eV). A schematic diagram of the charge distribution of the lowest dipole mode, $(k,l) = (0,\pm1)$, is drawn for each case, showing the form of the hybridized plasmon modes. Higher modes adopt similar hybridization behavior.

where

$$H(x) = \frac{\sinh(\hbar x/k_B T)}{\cosh(E_f/k_B T) + \cosh(\hbar x/k_B T)}.$$

Here, e is the elementary charge, $\hbar$ is the reduced Planck constant, E_f is the Fermi level of electrons above the Dirac point, ω is the angular frequency, and τ is the impurity-limited lifetime. Electrical gating can produce a Fermi level up to 1 eV [24]. The first term on the right-hand side corresponds to the contribution from intraband transitions, and the second term corresponds to the contribution from interband transitions. Interband transitions play a role for photon energies $\hbar\omega > 2E_f$. The impurity-limited lifetime can be estimated as $\tau = \mu E_f/ev_f^2$, where μ is the electron mobility and $v_f = 10^6$ m/s is the Fermi velocity [24]. Unless stated otherwise, we consider a mobility of 10 000 cm^2/V s, which is a conservative value compared with the largest mobilities measured for high-quality suspended graphene ($\mu > 15\,000$ cm^2/V s) [35].

The near-field interaction between two graphene disks is calculated under the electrostatic approximation [36]. The solution is obtained by expanding the surface charge using an orthogonal basis and then considering the boundary conditions at the surface of each disk [see Sec. S1 of the supplemental material (SM) [37]]. Using the fluctuation-dissipation theorem [38], we express the radiative thermal conductance between two objects 1 and 2 in terms of the surface charge expansion elements as

$$G_{NF} = \int_0^\infty \Phi_{12}(\omega)\hbar\omega \frac{df_{BE}}{dT} d\omega. \quad (2)$$

Here, f_{BE} is the Bose-Einstein distribution and $\Phi_{12}(\omega)$ is the ensemble-averaged flux spectrum (Sec. S2), which is given by

$$\Phi_{12}(\omega) = \frac{1}{2\pi}\mathrm{Tr}\left[\mathbf{G}^1_{AH}\mathbf{W}^*\mathbf{G}^2_{AH}\mathbf{W}\right]. \quad (3)$$

Here, Tr[·] is the trace of the matrix, $\mathbf{W} = 2[\mathbf{G}^1 + \mathbf{G}^2 + \mathbf{G}^0]^{-1}$ is the electrostatic polarization matrix, $\mathbf{G}^\nu$ and $\mathbf{G}^0$ are interaction matrices in the disk ν ($\nu = 1,2$) and in the surrounding media [Eqs. (S7) and (S8)], and $\mathbf{G}_{AH} = \frac{1}{2}(\mathbf{G} - \mathbf{G}^*)$ is the anti-Hermitian part of $\mathbf{G}$. As shown in Appendix, our theory and numerical simulations using the BEM show good agreement for frequencies below 80 THz.

III. RESULTS AND DISCUSSION

A. Plasmonic hybridization in graphene disk dimers

Localized surface plasmons in an isolated graphene disk can be classified by radial ($k = 0,1,\ldots$) and angular ($l = 0,\pm1,\pm2,\ldots$) indices [29]. In Fig. 1(a), the normalized electric field in the direction perpendicular to the plane of a disk, $E_z/|E_z|_{\max}$, for the $(k,l) = (0,\pm1)$, $(0,\pm2)$, $(1,\pm1)$, and $(1,\pm2)$ modes is shown for a disk diameter, D, of 100 nm and a Fermi level of 0.6 eV. The surface charge for modes with $k = 0$ is mostly distributed along the edge of the disk, while for $k = 1$ (and higher, not shown) the charge is distributed across the surface.

When two disks are separated by a small gap, the overall electromagnetic response differs from the response of an isolated disk. This phenomenon is known as surface plasmon hybridization and is a consequence of the near-field interaction between nanostructures [39,40]. In the case of two coaxial graphene disks separated by a distance Δz, each fundamental

mode hybridizes into a higher-frequency mode and a lower-frequency mode, as shown in Fig. 1(b) for $(k,l) = (0,\pm 1)$ and $(0,\pm 2)$. The high- and low-frequency modes are characterized by the charges on each disk oscillating in-phase and out-of-phase [28,39]. In the limit of $\Delta z/D \ll 1$, the frequencies of the hybridized modes saturate. The highest-frequency mode reaches $\sqrt{2}\omega_0$, where ω_0 is the resonant frequency of the nonhybridized mode [39]. The value of $\Delta z/D$ where the hybridization begins and the size of the frequency shifts in the limit of small separation are different for each fundamental mode.

In the case of two coplanar disks with center-to-center disk distance Δx, breaking the axial symmetry produces four hybrid modes for each fundamental mode, as shown in Fig. 1(c) for $(k,l) = (0,\pm 1)$ and $(0,\pm 2)$. The two central hybrid modes have charges oscillating perpendicular to the Δx axis, with similar characteristics to those of the coaxial hybrid modes. The other two modes have charges oscillating along the Δx axis. The resonant frequency is highest when the charges oscillate out-of-phase and lowest when the charges oscillate in-phase.

B. Near-field radiation in coaxial disk dimers

Surface plasmon hybridization plays a major role in near-field radiative heat transfer between two graphene disks. We evaluate the near-field radiative heat transfer enhancement as $G_{\rm NF}/G_{\rm BB}$. $G_{\rm NF}$ is the near-field radiative thermal conductance obtained from Eq. (2), and $G_{\rm BB}$ is the blackbody radiative thermal conductance between one side of a graphene disk and an infinite surface [41],

$$G_{\rm BB} = \sigma_{\rm SB} T^3 \pi D^2, \tag{4}$$

where $\sigma_{\rm SB}$ is the Stefan-Boltzmann constant. Here and in all subsequent calculations, we consider a temperature of 300 K. As a reference, $G_{\rm BB}$ is 4.8×10^{-2} pW/K for a disk of 100 nm diameter.

The near-field enhancement between two suspended coaxial graphene disks of 100 nm diameter and a Fermi level of 0.6 eV is plotted in Fig. 2 as a function of their separation. Three regimes can be distinguished: (i) a weak-coupling regime at large separations, where the response scales as $(\Delta z)^{-6}$, similar to the interaction between two small dipoles [4]; (ii) a strong-coupling limit at narrow gaps that scales as $(\Delta z)^{-1}$; and (iii) a transition regime in between. The deviation from the $(\Delta z)^{-6}$ scaling in the strong-coupling and transition regimes is a result of the near-field interaction between nanostructures [6,42] and is indicative of the presence of surface plasmon hybridization. For $\Delta z/D < 3.7$, near-field radiative heat transfer exceeds the blackbody limit, reaching values three orders of magnitude larger when $\Delta z/D = 0.01$.

The role played by hybridization is different in the strong-coupling and transition regimes. In the strong-coupling regime, the shifts in the hybrid frequencies of each mode have reached their limit, as mentioned in Sec. III A. In this regime, the near-field thermal conductance scales as $(\Delta z)^{-1}$, which is the same trend as for near-field radiation between two infinite parallel plates [43]. This result indicates that surface mode coupling is dominant. Near-field enhancement in the transition regime, on the other hand, is dominated by the

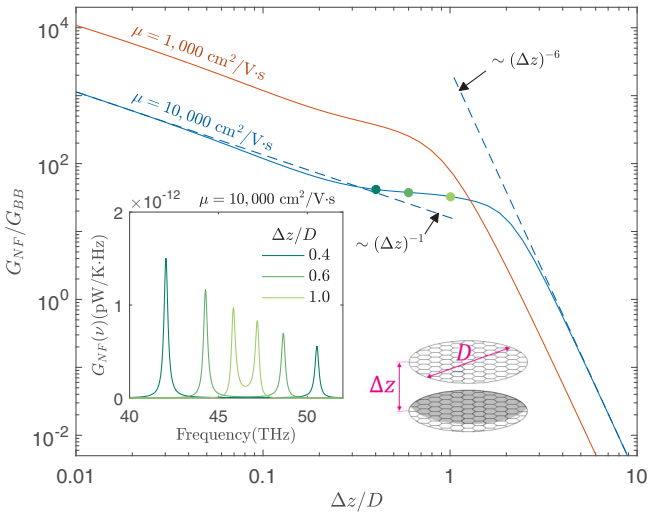

FIG. 2. Near-field enhancement, $G_{\rm NF}/G_{\rm BB}$, of two coaxial graphene disks as a function of their separation ($D = 100$ nm, $E_f = 0.6$ eV). Inset: spectral radiative thermal conductance, $G_{\rm NF}(\nu)$, showing the hybridization of the fundamental dipole mode $(k,l) = (0,\pm 1)$ at $\Delta z/D = 0.4$, 0.6, and 1.0.

shifting of the resonant frequencies, where interactions from the disk edges play the major role [39]. This phenomenon is observed in the spectral thermal conductance, $G_{\rm NF}(\nu)$, plotted in the inset of Fig. 2 for $\Delta z/D = 0.4$, 0.6, and 1.0 for the lowest dipole mode, $(k,l) = (0,\pm 1)$. The peaks are the result of resonances of the hybrid modes and separate as Δz decreases. Higher-order modes present a similar behavior. The shift of the resonant frequencies creates competing effects between a higher thermal activation of the redshifted hybrid modes and a lower thermal activation of the blueshifted hybrid modes.

To investigate the effects of optical losses in near-field radiation enhancement, we also considered a mobility of 1000 cm^2/V s. The resulting $G_{\rm NF}/G_{\rm BB}$ is plotted in Fig. 2. When $\Delta z/D \gg 1$, the near-field enhancement is lower than the case with $\mu = 10\,000$ cm^2/V s. In this regime, the dipole approximation is valid [5,6] and the near-field thermal conductance between two nanostructures with electric polarizability α and separated a distance d is [4]

$$G_{\rm NF} \propto \int_0^\infty \frac{[{\rm Im}(\alpha)]^2}{d^6} \hbar\omega \frac{df_{\rm BE}}{dT} d\omega.$$

When optical losses increase, the peak in ${\rm Im}(\alpha)$ decays, reducing the near-field enhancement. For $\Delta z/D < 1$, the near-field enhancement is larger compared to the results for a mobility of 10 000 cm^2/V s, indicating that near-field radiation is dominated by optical losses. In the strong-coupling regime ($\Delta z/D \ll 1$), near-field enhancement remains larger compared to the result for the larger mobility, and the ratio between the two curves is constant. At $\Delta z/D = 0.01$, the near-field thermal conductance exceeds the blackbody limit by four orders of magnitude. The behavior in this regime is consistent with the theory of near-field radiation between two semi-infinite surfaces, where higher optical losses favor near-field enhancement [44].

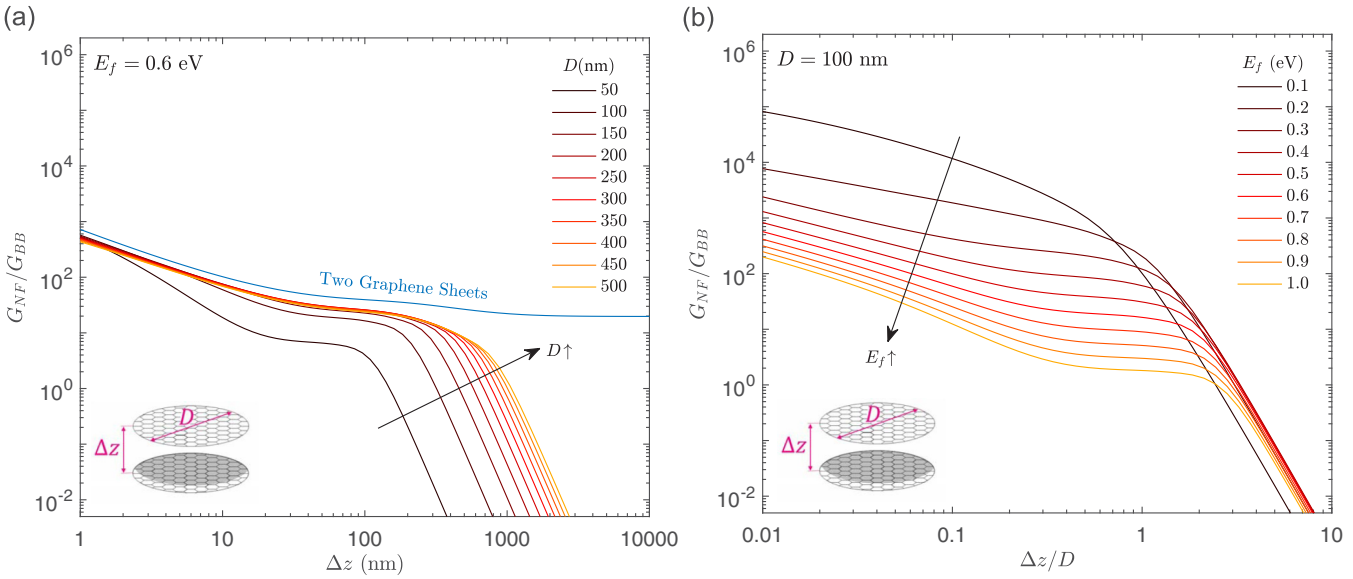

FIG. 3. (a) Near-field radiation enhancement between two coaxial graphene disks ($E_f = 0.6$ eV) as a function of the distance Δz for disk diameters ranging from 50 to 500 nm. The blue line represents the near-field enhancement between two graphene sheets [17] with $E_f = 0.6$ eV. (b) Near-field radiation enhancement between two coaxial graphene disks ($D = 100$ nm) as a function of the distance Δz for Fermi levels ranging from 0.1 to 1.0 eV.

The near-field enhancement between two coaxial graphene disks as a function of Δz for disk diameters ranging from 50 to 500 nm is plotted in Fig. 3(a). The top line represents the near-field enhancement of two suspended infinite parallel graphene sheets, obtained from the model of Ref. [17]. The near-field enhancement increases monotonically with increasing disk diameter in the weak-coupling regime. In the strong-coupling regime, the near-field enhancement approaches the limit given by the parallel graphene sheets. As the disk diameter increases, the transition points between the three regimes are shifted to larger values of Δz, in agreement with other studies of near-field radiation between nanoparticles [6,42].

In Fig. 3(b), the near-field enhancement between two coaxial graphene disks as a function of $\Delta z/D$ is plotted for a Fermi level ranging from 0.1 to 1.0 eV. All the curves show a similar trend in the weak-coupling regime, followed by an increased near-field enhancement in the strong-coupling regime as the Fermi level decreases. Lowering the Fermi level has two effects: (i) optical losses are increased due to higher rates of intraband and interband transitions, and (ii) the resonant frequencies are redshifted [45], which increases the contribution from f_{BE}. In the strong-coupling regime, the two effects both lead to larger near-field enhancement as E_f is reduced. In the weak-coupling regime, where optical losses are unfavorable for near-field enhancement, the two effects compete and the curves overlap for different values of E_f. Due to the different role played by optical losses in the strong- and weak-coupling regimes, the curves cross in the transition regime.

As can be seen in Figs. 2, 3(a), and 3(b), the length scales that determine the limits of the strong-coupling, transition, and weak-coupling regimes depend on D, E_f, and μ. As shown in Sec. S3 of the SM, for $\hbar\omega/E_f < 1$, low temperatures ($k_{\mathrm{B}}T/E_f \ll 1$), and low optical losses ($\omega_R^{-1}\tau^{-1} \ll 1$, valid when $\mu = 10\,000$ cm^2/V s), a nondimensional thermal conductance for a general case of two parallel disks can be written in terms of three nondimensional parameters as

$$\frac{G_{\mathrm{NF}}}{k_{\mathrm{B}}\omega_R} = f\left(\frac{\Delta z}{D}, \frac{\Delta x}{D}, \frac{k_{\mathrm{B}}T}{\hbar\omega_R}\right), \tag{5}$$

where $k_{\mathrm{B}}T/\hbar\omega_R$ is the nondimensional temperature and

$$\omega_R = \sqrt{\frac{2E_f e^2}{\hbar^2 \varepsilon_0 \varepsilon_h D}} \tag{6}$$

is the characteristic plasmon frequency. Here ε_0 is the vacuum permittivity and $\varepsilon_h = (\varepsilon_1 + \varepsilon_2)/2$, where ε_1 and ε_2 are the dielectric constants of the media that bound the graphene disks.

For the case of coaxial disks (i.e., $\Delta x/D = 0$), $G_{\mathrm{NF}}/k_{\mathrm{B}}\omega_R$ is plotted as a function of $\Delta z/D$ in Fig. 4 for $\hbar\omega_R/k_{\mathrm{B}}T = 5$, 9, and 15. These $\hbar\omega_R/k_{\mathrm{B}}T$ values were chosen in accordance with the range of disk diameters (50–500 nm) and the temperature (300 K) considered in this work. The red dash-dotted lines mark the limits between the strong-coupling and transition regimes, $(\Delta z/D)_{s\text{-}t}$, and between the transition and weak-coupling regimes, $(\Delta z/D)_{t\text{-}w}$. These two limits correspond to where the curves deviate by more than 0.2% from $(\Delta z)^{-1}$ or $(\Delta z)^{-6}$ scalings. The three curves deviate from the dipole-dipole scaling of the weak-coupling regime at approximately the same point, $(\Delta z/D)_{t\text{-}w} \approx 3.2$. This point corresponds to where the hybridization of the fundamental dipole mode [$(k,l) = (0,\pm 1)$] begins.

On the other hand, $(\Delta z/D)_{s\text{-}t}$ depends on $\hbar\omega_R/k_{\mathrm{B}}T$. This behavior can be understood by considering the origin of the $(\Delta z)^{-1}$ scaling, which begins when all the thermally active hybrid modes have reached their maximum frequency shift. As mentioned in Sec. III A, this limit is different for each fundamental mode. Thus, the value of $(\Delta z/D)$ for the maximum frequency shift depends on the hybrid mode populations, which are determined by $\hbar\omega_R/k_{\mathrm{B}}T$. As plotted in the inset to Fig. 4, $(\Delta z/D)_{s\text{-}t} \approx 0.02$ for $5 < \hbar\omega_R/k_{\mathrm{B}}T < 7$ and $11 <$

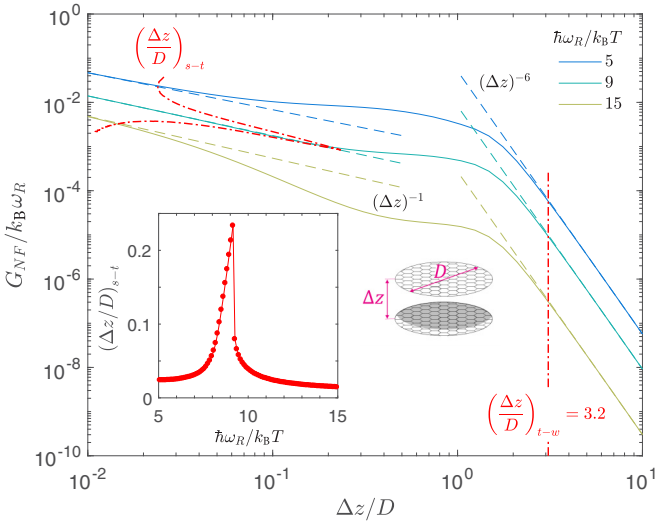

FIG. 4. Nondimensional thermal conductance $G_{NF}/k_B\omega_R$ as a function of $\Delta z/D$. The red dash-dotted lines mark the limits between the strong-coupling and transition regimes, $(\Delta z/D)_{s\text{-}t}$, and between transition and weak-coupling regimes, $(\Delta z/D)_{t\text{-}w}$. Here, $(\Delta z/D)_{t\text{-}w} \approx 3.2$. In the inset, $(\Delta z/D)_{s\text{-}t}$ is plotted as a function of $\hbar\omega_R/k_BT$, where the line serves as a guide to the eye.

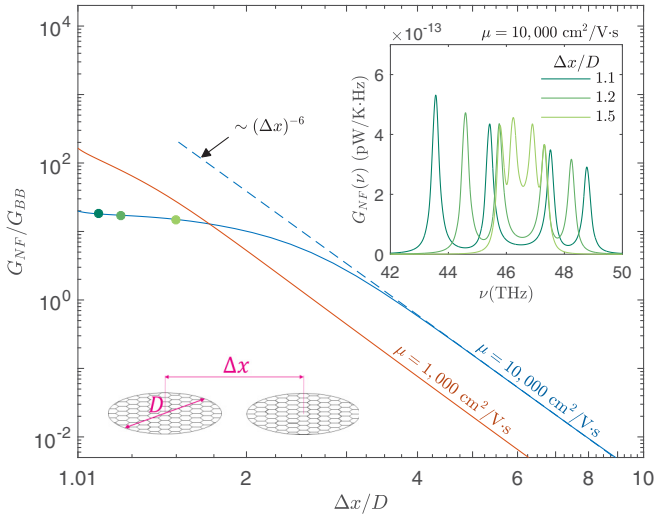

FIG. 5. Near-field enhancement for two coplanar graphene disks at different gaps ($D = 100$ nm, $E_f = 0.6$ eV). Inset: Spectral radiative thermal conductance showing the hybridization of the lowest dipole mode $(k,l) = (0,\pm1)$ at $\Delta x/D = 1.1$, 1.2, and 1.5.

$\hbar\omega_R/k_BT < 15$. For $7 < \hbar\omega_R/k_BT < 11$, a sharp peak is observed that reaches a maximum of 0.23 at $\hbar\omega_R/k_BT = 9.2$.

C. Near-field radiation in coplanar disk dimers

We now consider the near-field radiative heat transfer enhancement G_{NF}/G_{BB} between two coplanar disks. To be consistent with the analysis from Sec. III B, G_{BB} is taken to be the blackbody radiation thermal conductance between the surface of one disk and an infinite surface [Eq. (4)]. The blackbody radiation heat exchange between the disk's edge and an infinite surface is given by [41]

$$G_{BB}^{edge} = 8\pi\sigma_{SB}T^3Dt, \tag{7}$$

where t is the thickness of a graphene layer, which we take to be 0.5 nm based on previous studies on graphene plasmonic nanostructures [45,46]. We note that studies of thermal transport in graphene often use a thickness of 0.34 nm, which is based on the layer separation in graphite [47,48]. For a disk diameter of 100 nm, $G_{BB}^{edge} = 1.9 \times 10^{-6}$ pW/K, which is 25 times smaller than G_{BB}.

The near-field enhancement is also strong for two coplanar disks, as plotted in Fig. 5, where the thermal conductance exceeds the blackbody limit by a factor of 10 when the gap is small. Lower-quality graphene ($\mu = 1000$ cm^2/V s) shows a larger near-field enhancement only when $\Delta x/D < 2$. The near-field radiation follows three regimes, similar to the case of two coaxial disks. Given the scaling of the plot, only the weak and transition regimes can be distinguished. In the inset, the spectral data for $(k,l) = (0,\pm1)$ for $\Delta x/D = 1.1$, 1.2, and 1.5 show that each fundamental localized surface plasmon mode is hybridized into four modes due to the breaking of axial symmetry, as explained by Fig. 1(c). At large separations, the thermal conductance reaches the weak-coupling regime, where it scales as $(\Delta x)^{-6}$. By applying the nondimensional analysis, the limit between the transition and weak-coupling regimes occurs at $\Delta x/D \approx 3.2$ for $\mu = 10\,000$ cm^2/V s (Fig. S4). This value is the same as that found for the coaxial disks because the disks are effectively point dipoles in the weak-coupling regime.

D. Mismatched diameters

The effect of breaking the dimer symmetry is now investigated. Two coaxial disks with diameters D_1 and D_2 are considered by comparing the thermal conductance of a heterodimer ($D_2/D_1 \neq 1$) to a homodimer ($D_2/D_1 = 1$). The heterodimer/homodimer thermal conductance ratio, $G_{NF}/G_{NF}^{D_2/D_1=1}$, is plotted in Fig. 6(a) as a function of D_2/D_1 for $\Delta z/D_1 = 0.1$, 0.4, 0.6, 1.0, and 1.5; $D_1 = 100$ nm; and $50 < D_2 < 150$ nm. The results are asymmetric with respect to $D_2/D_1 = 1$. The thermal conductance for a diameter ratio of $D_2/D_1 = 1 + \delta$ is always greater than that for the diameter ratio of $1 - \delta$. In most cases, breaking the symmetry reduces the thermal conductance compared to the homodimer. For a given D_2/D_1, as $\Delta z/D_1$ decreases, $G_{NF}/G_{NF}^{D_2/D_1=1}$ increases. At $\Delta z/D = 0.4$ (0.1), the curves show an enhancement of thermal conductance of up to 4% (15%) in the domain $1.0 < D_2/D_1 \leqslant 1.2$ ($1.0 < D_2/D_1 \leqslant 1.6$). This enhancement is the result of a relaxation in the selection rules for hybridization, which increases the coupling between all modes [49]. The increased coupling adds additional channels for near-field thermal radiation. In the strong-coupling regime (not shown), the near-field thermal conductance is not affected by a diameter mismatch, and $G_{NF}/G_{NF}^{D_2/D_1=1} = 1$ for all values of D_2/D_1.

The spectral thermal conductances of heterodimers with $D_2/D_1 = 0.8$, 1.0, and 1.2, and $\Delta z/D = 1.5$, 0.6, and 0.1, are plotted in Fig. 6(b). $\Delta z/D = 1.5$ is close to the weak-coupling regime, and only a few modes participate in the coupling. Thus, a small mismatch in the disk diameters reduces the mode coupling and strongly suppresses the thermal conductance. $\Delta z/D = 0.6$ lies in the transition regime. Here,

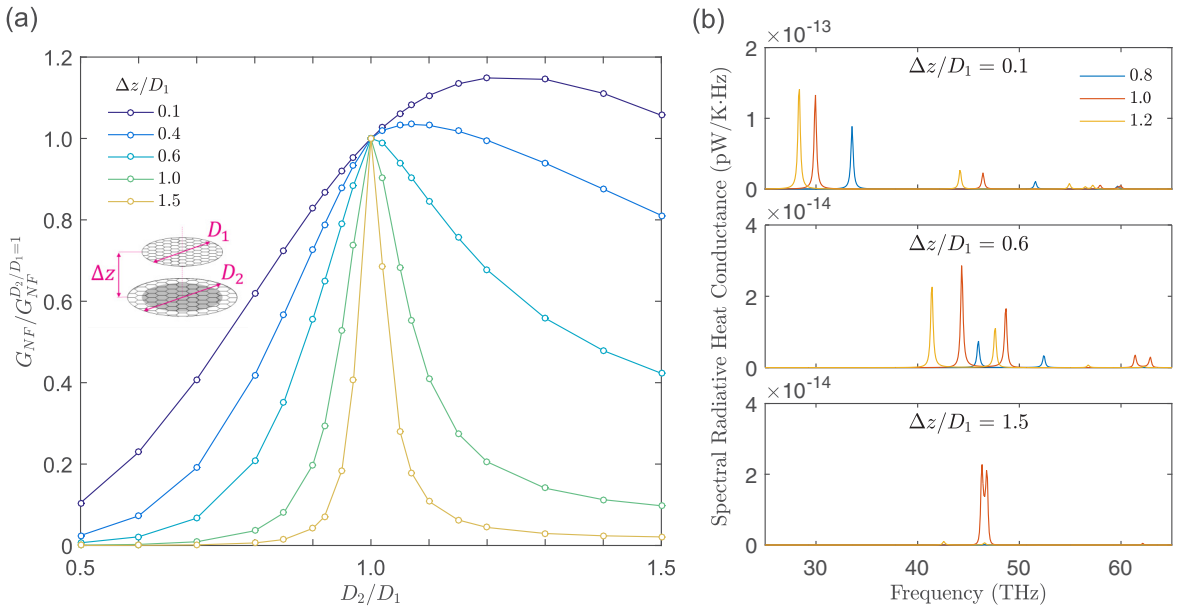

FIG. 6. Effect of breaking symmetry in the disk diameters on the thermal conductance of the coaxial configuration. (a) Relative thermal conductance of a heterodimer with respect to that of a homodimer for $D_1 = 100$, $50 < D_2 < 150$ nm. (b) Spectral thermal conductance of the heterodimer for selected cases.

the near-field coupling is stronger, allowing more modes to interact. As a consequence, for $D_2/D_1 < 1$ some peaks are blueshifted, and for $D_2/D_1 > 1$ some peaks are redshifted. $\Delta z/D = 0.1$ is close to the strong-coupling regime. In this case, for $D_2/D_1 > 1$, the majority of the peaks are redshifted, increasing the population with respect to the case $D_2/D_1 = 1$. This increase in population explains the thermal conductance enhancement over the homodimer case, as seen in Fig. 6(a). A similar behavior is observed for coaxial disk heterodimers (Sec. S4).

E. Parallel disk dimers at different positioning angles

As seen in Figs. 2 and 5, near-field interactions are conditioned by the distance between the two disks and their relative positions. To explore the transition between the coplanar and coaxial configurations, in Fig. 7(a) we plot the near-field enhancement between two parallel disks as a function of the positioning angle between centers, θ, for center-to-center separations, Δr, of 105, 120, and 150 nm. As in Figs. 2 and 5, $D = 100$ nm and $E_f = 0.6$ eV. By changing the angle between the two disks, a minimum is observed at $\theta \approx 48^\circ$ as they

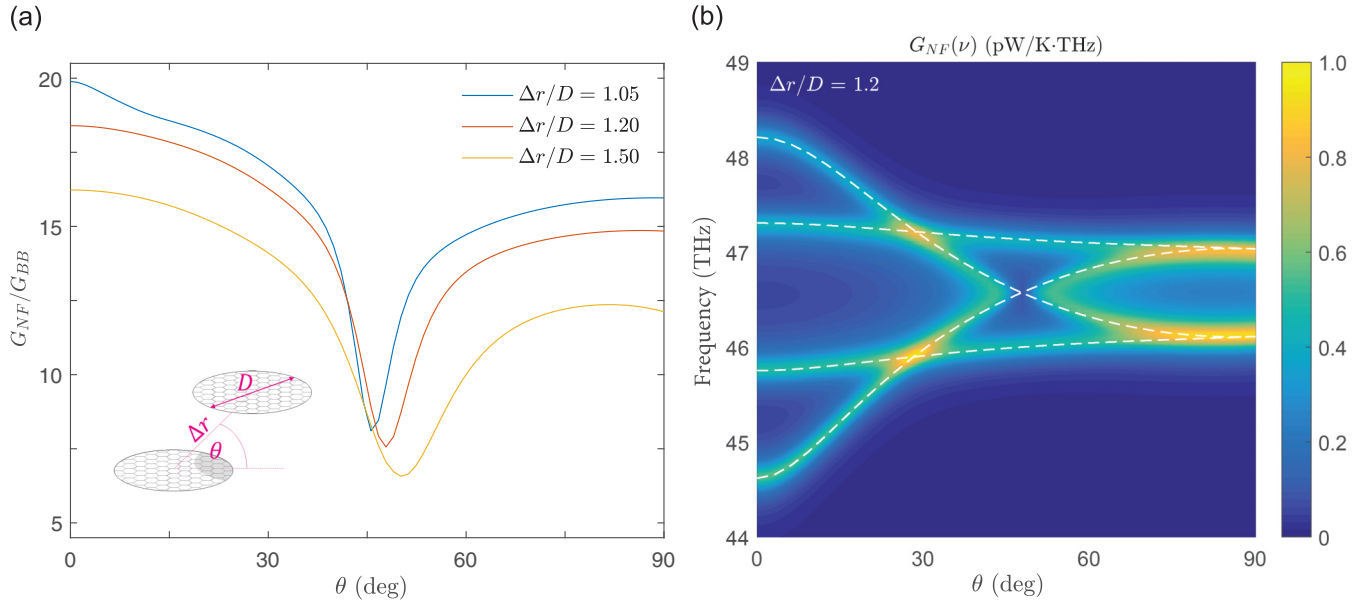

FIG. 7. Near-field enhancement, $G_{\mathrm{NF}}/G_{\mathrm{BB}}$, between two parallel graphene disks as a function of the positioning angle between centers θ, for center-to-center separations, Δr, of 105, 120, and 150 nm ($D = 100$ nm, $E_f = 0.6$ eV). (b) Spectral radiative thermal conductance at $\Delta r = 120$ nm showing the hybridization of the fundamental dipole mode, $(k,l) = (0,\pm 1)$, as a function of the angle.

transition between the coplanar and coaxial orientations. The spectral thermal conductance at a separation of 120 nm is plotted in Fig. 7(b) for the lowest dipole mode $(k,l) = (0,\pm 1)$ for $0^\circ \leqslant \theta \leqslant 90^\circ$, revealing the role played by surface plasmon hybridization. The hybridized resonant frequencies transition from four modes at $\theta = 0^\circ$ to two twofold-degenerate modes at $\theta = 90^\circ$. At $\theta = 48^\circ$, two of the hybrid modes have the same resonant frequency, producing destructive interference and reducing the thermal conductance. This angle corresponds to the minimum in the near-field enhancement in Fig. 7(a).

IV. CONCLUSIONS

We developed an electrostatic semianalytical approach that is a powerful tool for fast modeling of near-field radiation in graphene nanostructures. Its application to two coaxial graphene disks demonstrates that near-field coupling can lead to up to four orders of magnitude enhancement of radiative heat transfer beyond the blackbody limit, as shown in Fig. 2. Three regimes were observed: a strong-coupling regime and a transition regime for small separations, which are dominated by surface plasmon hybridization, and a weak-coupling regime for larger separations that is dominated by dipole interactions. In the strong-coupling regime, the near-field enhancement follows the trend of two infinite graphene sheets. Larger optical losses increase near-field thermal conductance in the transition and strong-coupling regimes, while they are detrimental in the weak-coupling regime. The near-field enhancement depends strongly on the disk diameter [Fig. 3(a)] and the Fermi level [Fig. 3(b)].

Using nondimensional analysis, we derived a universal function for the near-field thermal conductance. For the coaxial disk configuration, the nondimensional model was used to identify where the thermal conductance deviates from the weak-coupling and strong-coupling regimes (Fig. 4). These results indicate when the electrostatic model can be replaced by less complex approximate models (i.e., the dipole-dipole approximation in the weak-coupling regime and the infinite graphene sheet approximation in the strong-coupling regime).

The coupling between two coaxial disks is also strong, as shown in Fig. 5, with two orders of magnitude enhancement of radiative heat transfer beyond the blackbody limit. The result for coplanar disks is particularly interesting, as classical theories for far-field radiation predict negligible heat transfer rates due to the small view factor. Varying the relative position between the disks while keeping them parallel can induce destructive interference between hybrid modes, which dramatically reduces the radiative heat transfer rate (Fig. 7).

A future experimental validation of the results presented here would need to consider scenarios in which (i) the symmetry of the two disks cannot be maintained due to mismatch in the diameters, Fermi levels, or optical losses induced by defects; and (ii) the coupling of surface plasmons with optical phonons in the substrate(s). In most of the cases we considered, near-field radiation between disks with mismatched diameters showed a reduction of the near-field thermal conductance from that of the symmetrical disk dimer (Figs. 6 and S5). We observed some cases, however, in which the near-field thermal conductance of the heterodimer exceeds that of the homodimer due to the relaxation in the selection rules for plasmon hybridization. Thus, the net effect of the mismatch between disks must be evaluated for individual cases.

Yan *et al.* experimentally observed that the presence of optical phonons can induce higher losses of surface plasmons in nanostructured graphene as well as additional peaks due to hybridization [50]. Both of these elements can increase the near-field enhancement, as theoretically demonstrated in extended graphene sheets on a SiO_2 substrate [19]. Thus, under certain conditions, the presence of optical phonons can lead to an enhancement of near-field radiation. The electrostatic approximation cannot be applied when surface plasmons interact with substrate optical phonons. In this case, computational electrodynamics tools are required.

Our findings demonstrate the potential of graphene nanostructures for tunable near-field radiation enhancement, paving the way for the development of graphene metamaterials and photon-based thermal solid-state devices. Coplanar nanodisk waveguides in particular have the potential for tunable plasmonic heat transport. This concept is explored in the following paper [51].

ACKNOWLEDGMENTS

This work was supported by Comisión Nacional de Investigación Científica y Tecnológica (CONICYT), Becas de Doctorado en el Extranjero BECAS CHILE.

APPENDIX: VALIDATION OF ELECTROSTATIC MODEL FOR NEAR-FIELD RADIATION

The flux spectrum between two coaxial disks ($\Delta z = 50$ nm) and two coplanar disks ($\Delta x = 110$ nm) obtained using our electrostatic semianalytical model and from numerical simulations using the BEM-based software package SCUFF-EM [30] is plotted in Figs. 8(a) and 8(b). The black line connecting the green circles serves as a guide to the eye. For the BEM simulations, we considered disks with a small thickness, $t = 1$ nm, and an effective dielectric constant for graphene, $\varepsilon_g = 1 - \frac{\sigma(\omega)}{i\omega\varepsilon_0 t}$ [34], where ε_0 is the permittivity of free space. Because of the finite thickness, the BEM predictions are redshifted by 13% from the curves obtained by the electrostatic model. These shifts are corrected in Figs. 8(a) and 8(b) in order to compare the two methods.

Good agreement is observed in both geometries for frequencies bellow 80 THz. At higher frequencies, the contribution of $\Phi(\omega)$ to the overall radiative thermal conductance is less than 4% due to the form of the Bose-Einstein distribution. The results from our theory were obtained two orders of magnitude faster than those from the BEM simulations (10 800 s computation time for the BEM simulation versus 31 s for the semianalytical model using one six-core Intel Xeon X5690 processor at 3.47 GHz).

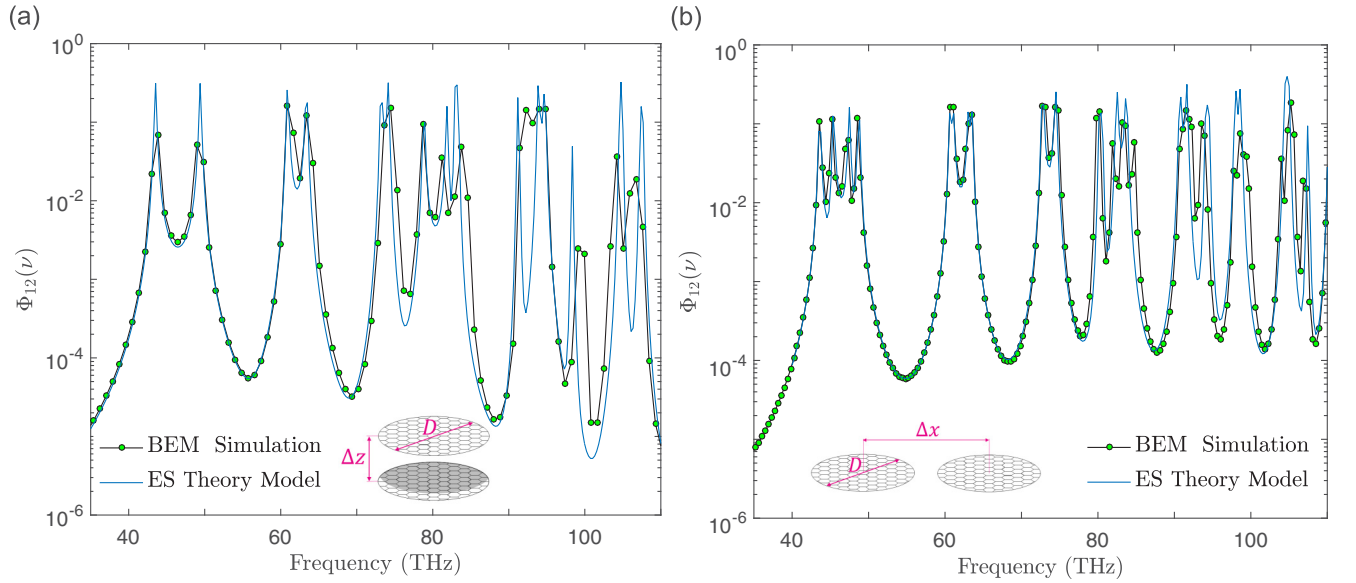

FIG. 8. Comparison of our electrostatic semianalytical model and BEM simulations for the flux spectrum of two graphene disks ($D = 100$ nm, $E_f = 0.6$ eV) in (a) a coaxial configuration with $\Delta z = 50$ nm, and (b) a coplanar configuration with $\Delta x = 110$ nm. The black line connecting the green circles serves as a guide to the eye.

[1] K. Joulain, J. P. Mulet, F. Marquier, R. Carminati, and J. J. Greffet, Surf. Sci. Rep. **57**, 59 (2005).

[2] B. Song, Y. Ganjeh, S. Sadat, D. Thompson, A. Fiorino, V. Fernández-Hurtado, J. Feist, F. J. Garcia-Vidal, J. C. Cuevas, P. Reddy, and E. Meyhofer, Nat. Nanotechnol. **10**, 253 (2015).

[3] S. Shen, A. Narayanaswamy, and G. Chen, Nano Lett. **9**, 2909 (2009).

[4] A. I. Volokitin and B. N. J. Persson, Phys. Rev. B **63**, 205404 (2001).

[5] G. Domingues, S. Volz, K. Joulain, and J. J. Greffet, Phys. Rev. Lett. **94**, 085901 (2005).

[6] A. Narayanaswamy and G. Chen, Phys. Rev. B **77**, 075125 (2008).

[7] A. Manjavacas and F. J. García de Abajo, Phys. Rev. B **86**, 075466 (2012).

[8] X. L. Liu, R. Z. Zhang, and Z. M. Zhang, Appl. Phys. Lett. **103**, 213102 (2013).

[9] B. Liu and S. Shen, Phys. Rev. B **87**, 115403 (2013).

[10] O. D. Miller, S. G. Johnson, and A. W. Rodriguez, Phys. Rev. Lett. **112**, 157402 (2014).

[11] S. A. Biehs, M. Tschikin, and P. Ben-Abdallah, Phys. Rev. Lett. **109**, 104301 (2012).

[12] L. Zhu, C. R. Otey, and S. Fan, Phys. Rev. B **88**, 184301 (2013).

[13] P. Ben-Abdallah, A. Belarouci, L. Frechette, and S.-A. Biehs, Appl. Phys. Lett. **107**, 053109 (2015).

[14] P. Ben-Abdallah and S. A. Biehs, Z. Naturforsch. A **72**, 151 (2017).

[15] P. Ben-Abdallah, Phys. Rev. Lett. **116**, 084301 (2016).

[16] R. Messina and P. Ben-Abdallah, Sci. Rep. **3**, 1383 (2013).

[17] O. Ilic, M. Jablan, J. D. Joannopoulos, I. Celanovic, H. Buljan, and M. Soljačić, Phys. Rev. B **85**, 155422 (2012).

[18] V. B. Svetovoy, P. J. van Zwol, and J. Chevrier, Phys. Rev. B **85**, 155418 (2012).

[19] A. I. Volokitin and B. N. J. Persson, Phys. Rev. B **83**, 241407 (2011).

[20] B. Liu, Y. Liu, and S. Shen, Phys. Rev. B **90**, 195411 (2014).

[21] R. Yu, A. Manjavacas, and F. J. García de Abajo, Nat. Commun. **8**, 2 (2017).

[22] T. Low and P. Avouris, ACS Nano **8**, 1086 (2014).

[23] A. N. Grigorenko, M. Polini, and K. S. Novoselov, Nat. Photon. **6**, 749 (2012).

[24] F. J. García de Abajo, ACS Photon. **1**, 135 (2014).

[25] S. Barzegar-Parizi, B. Rejaei, and A. Khavasi, IEEE J. Quantum Electron. **51**, 1 (2015).

[26] W. Wang, P. Apell, and J. Kinaret, Phys. Rev. B **84**, 085423 (2011).

[27] W. Wang, S. P. Apell, and J. M. Kinaret, Phys. Rev. B **86**, 125450 (2012).

[28] A. Kumar, K. H. Fung, M. T. Homer Reid, and N. X. Fang, Opt. Express **22**, 6400 (2014).

[29] A. L. Fetter, Phys. Rev. B **33**, 5221 (1986).

[30] M. T. H. Reid, SCUFF-EM: Free, open-source software for boundary-element analysis of problems in computational physics and engineering (2014).

[31] V. Fessatidis, H. L. Cui, and O. Kühn, Phys. Rev. B **47**, 6598 (1993).

[32] F. A. Reboredo and C. R. Proetto, Phys. Rev. B **53**, 12617 (1996).

[33] V. Cataudella and G. Iadonisi, Phys. Rev. B **35**, 7443 (1987).

[34] L. A. Falkovsky, J. Phys. Conf. Ser. **129**, 012004 (2008).

[35] A. K. Geim and K. S. Novoselov, Nat. Mater. **6**, 183 (2007).

[36] C. F. Bohren and D. R. Huffman, *Absorption and Scattering of Light by Small Particles* (Wiley-VCH, Weinheim, Germany, 1998), p. 544.

[37] See Supplemental Material at http://link.aps.org/supplemental/10.1103/PhysRevB.96.165427 for details of the electrostatic theory of graphene nanodisks, the flux spectrum model,

and nondimensional analysis, and results of nondimensional thermal conductance and mismatched disk analysis for co-planar disks. The supplemental material includes Refs. [24,26,28,29,38,51-54].

[38] G. Agarwal, Phys. Rev. A **11**, 230 (1975).

[39] F. Ramirez, B. Liu, and S. Shen, J. Quant. Spectrosc. Radiat. Transf. **158**, 27 (2015).

[40] T. J. Davis, K. C. Vernon, and D. E. Gómez, Phys. Rev. B **79**, 155423 (2009).

[41] A. S. Lavine, D. P. DeWitt, T. L. Bergman, and F. P. Incropera, *Fundamentals of Heat and Mass Transfer* (Wiley, New York, 2011), p. 1080.

[42] S. Xiong, K. Yang, Y. A. Kosevich, Y. Chalopin, R. D'Agosta, P. Cortona, and S. Volz, Phys. Rev. Lett. **112**, 114301 (2014).

[43] P. Rodriguez-López, W.-K. Tse, and D. A. R. Dalvit, J. Phys. Condens. Matter **27**, 214019 (2015).

[44] J. P. Mulet, K. Joulain, R. Carminati, and J. J. Greffet, Microscale Thermophys. Eng. **6**, 209 (2002).

[45] F. H. L. Koppens, D. E. Chang, and F. J. García de Abajo, Nano Lett. **11**, 3370 (2011).

[46] J. Christensen, A. Manjavacas, S. Thongrattanasiri, F. H. L. Koppens, and F. J. G. de Abajo, ACS Nano **6**, 431 (2012).

[47] A. A. Balandin, Nat. Mater. **10**, 569 (2011).

[48] S. Lu and A. J. H. McGaughey, J. Appl. Phys. **121**, 115103 (2017).

[49] L. V. Brown, H. Sobhani, J. B. Lassiter, P. Nordlander, and N. J. Halas, ACS Nano **4**, 819 (2010).

[50] H. Yan, F. Xia, Z. Li, and P. Avouris, New J. Phys. **14**, 125001 (2012).

[51] F. V. Ramirez and A. J. H. McGaughey, Phys. Rev. B **96**, 165428 (2017).

[52] J. D. Jackson, *Classical Electrodynamics*, 3rd ed. (Wiley, New York, 1998), p. 832.

[53] I. S. Gradshteyn and I. M. Ryzhik, *Table of Integrals, Series, and Products*, 7th ed., edited by A. Jeffrey and D. Zwillinger (Academic Press, New York, 2007), p. 1200.

[54] L. Tsang, J. A. Kong, K.-H. Ding, and C. O. Ao, *Scattering of Electromagnetic Waves: Theories and Applications* (Wiley-Interscience, New York, 2000), p. 445.